Geophysical Journal International

Geophys. J. Int. (2019) **219,** 2174–2186
Advance Access publication 2019 October 03
GJI Seismology

doi: 10.1093/gji/ggz434

Crustal structure variations in south-central Mexico from receiver functions

Miguel Rodríguez-Domínguez [1], Xyoli Pérez-Campos,[2] Conrado Montealegre-Cázares,[1] Robert W. Clayton [3] and Enrique Cabral-Cano[2]

[1] *Posgrado en Ciencias de la Tierra, Universidad Nacional Autónoma de México, Mexico City 04510, Mexico. E-mail: miguel.anrodo@gmail.com*
[2] *Instituto de Geofísica, Universidad Nacional Autónoma de México, Mexico City 04510, Mexico*
[3] *Seismological Laboratory, Department of Earth and Planetary Sciences, California Institute of Technology, 1200 E California Blvd, Pasadena, CA 91125, USA*

Accepted 2019 September 30. Received 2019 September 23; in original form 2019 April 11

SUMMARY

Mexico has a complex geological history that is typified by the distinctive terranes that are found in the south-central region. Crustal thickness variations often correlate with geological terranes that have been altered by several processes in the past, for example aerial or subduction erosion, underplating volcanic material or rifting but few geophysical studies have locally imaged the entire continental crust in Mexico. In this paper, the thickness of three layers of the crust in south-central Mexico is determined. To do this, we use *P*- and *S*-wave receiver functions (RF) from 159 seismological broad-band stations. Thanks to its adaptive nature, we use an empirical mode decomposition (EMD) algorithm to reconstruct the RFs into intrinsic mode functions (IMF) in order to enhance the pulses related to internal discontinuities within the crust. To inspect possible lateral variations, the RFs are grouped into quadrants of 90°, and their amplitudes are mapped into the thickness assuming a three-layer model. Using this approach, we identify a shallow sedimentary layer with a thickness in the range of 1–4 km. The upper-crust was estimated to be of a few kilometers (<10 km) thick near the Pacific coast, and thicker, approximately 15 km in central Oaxaca and under the Trans-Mexican Volcanic Belt (TMVB). Close to the Pacific coast, we infer a thin crust of approximately 16 ± 0.9 km, while in central Oaxaca and beneath the TMVB, we observe a thicker crust ranging between 30 and 50 km ± 2.0 km. We observe a crustal thinning, of approximately 6 km, from central Oaxaca (37 ± 1.9 km) towards the Gulf of Mexico, under the Veracruz Basin, where we estimate a crustal thickness of 31.6 ± 1.9 km. The boundary between the upper and lower crust in comparison with the surface of the Moho do not show significant variations other than the depth difference. We observe small crustal variations across the different terranes on the study area, with the thinnest crust located at the Pacific coast and Gulf of Mexico coast. The thickest crust is estimated to be in central Oaxaca and beneath the TMVB.

Key words: Structure of the Earth; Crustal imaging; Crustal structure.

1 INTRODUCTION

South-central Mexico has a long, varied and complicated geological history which is recorded in the contrasting terranes and their sedimentary cover exposed in Guerrero, Oaxaca, Puebla and Veracruz (Fig. 1). To illustrate, the Xolapa terrane resulted from the displacement of the Chortis Block and the resulting erosion of the margin and exhumation of the forearc (Morán-Centeno *et al.* 1996), while the Maya terrane resulted from the breakup of Pangea in the Middle-Jurassic and during the late Cretaceous-early Cenozoic it was amalgamated with southeastern Mexico (Sedlock *et al.* 1993).

A few studies have estimated the thickness and structure of the crust. For instance, Urrutia-Fucugauchi & Flores-Ruiz (1996) determined the regional crustal thickness beneath the Trans-Mexican Volcanic Belt (TMVB) and the surrounding area towards the Pacific coast and the Gulf of Mexico, using gravity data; in southern Mexico, Valdés *et al.* (1986) used seismic and gravity data to model the velocity structure of the crust in central Oaxaca, and Nava *et al.* (1988) along the Pacific coast in the same state. Iglesias *et al.* (2001) proposed an *S*-wave velocity, *Vs*, structure model by inverting dispersion curves with genetic algorithms and simulated annealing in Guerrero and Oaxaca; and, in a more recent study,

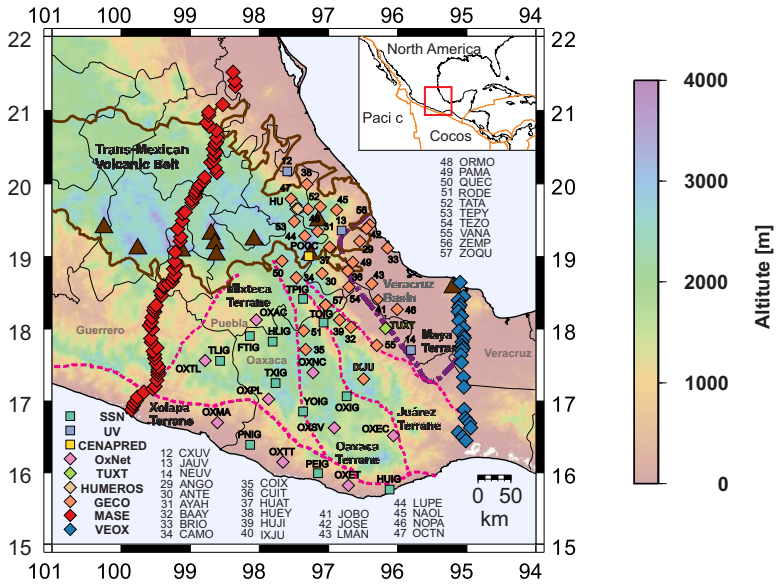

Figure 1. Location of the study area and seismic stations used. Dashed magenta lines show the boundaries from major geologic terranes in south-central Mexico (Ferrari *et al.* 2012). Other geologic provinces are shown as dash–dotted purple line for the Veracruz basin and solid brown for the Trans-Mexican Volcanic Belt (TMVB; Ferrari *et al.* 2012). The brown triangles denote active volcanos (Ferrari *et al.* 2012).

Ferrari *et al.* (2012) compiled the crustal thickness using the receiver functions results from the Meso-American Subduction Experiment (MASE, Pérez-Campos *et al.* 2008), the Mapping the Rivera Subduction Zone array (MARS, Yang *et al.* 2009) and the Veracruz-Oaxaca profile (VEOX, Melgar & Pérez-Campos 2011) along with the gravimetric data of Urrutia-Fucugauchi & Flores-Ruiz (1996). Espíndola *et al.* (2017), determined the crustal structure under each of the broad-band seismic stations of the Mexican National Seismological Service Network. In most of these studies, the crustal structure is limited to determining the depth of the Mohorovičić discontinuity (Moho). Some studies (e.g. Gaite *et al.* 2012; Spicka *et al.* 2016) have imaged the crust beneath Mexico using mainly cross-correlation techniques that are a few hundred kilometers away from each other. From another approach, Stubailo *et al.* (2012), by inverting phase velocity data, found differences on *Vs*, across south-central Mexico. They observe larger *Vs* in central Oaxaca in comparison with the values observed towards the Gulf of Mexico and the south. On this matter, Castellanos *et al.* (2018) estimated a 3-D *Vs* model from ambient seismic noise, near the TMVB and the Veracruz basin, where they observe a crustal thinning towards the Gulf of Mexico, previously recognized by Urrutia-Fucugauchi & Flores-Ruiz (1996). Despite all these works, there is a gap on data, information, and therefore, on the details of the crustal structure under the region formed by the states of Oaxaca, Puebla and Veracruz.

The purpose of this study is to analyse, in more detail, the crustal structure in south-central Mexico, its lateral variations and its relationship with some of the geological terranes of the region. An improved, or complementary, model of the crust in south-central Mexico, would be beneficial to reduce the uncertainty of depth estimation for regional earthquakes, which at regional distances is highly dependent on the velocity model; also, an accurate assessment of the crustal thickness will help addressing other important tectonic unknowns and controversies, such as the possible presence of a slab tear in the same region (e.g. Fasola *et al.* 2016; Castellanos *et al.* 2018). Furthermore, crustal thickness variations in so short distances as under the active volcanoes, east of the TMVB and the Veracruz basin, suggest the need for further detail tomography studies to delineate low-velocity anomalies associated with magmatic processes in the region.

P-wave receiver functions (PRF), which represent the relative response to impedance contrasts between elastic media (Ammon 1991), are usually employed to constrain the crustal thickness (Langston 1979; Ammon & Zandt 1993; Julià & Mejia 2004; Chen *et al.* 2010; Ozakin & Ben-Zion 2015). Although *S*-wave receiver functions (SRF) have been used previously to image deeper discontinuities within the Earth (e.g. Farra & Vinnik 2000; Zhou *et al.* 2000; Vinnik *et al.* 2017), they have not been used as routinely as PRF because of their lower frequencies.

Crustal structure studies in south-central Mexico (Kim *et al.* 2010; Melgar & Pérez-Campos 2011; Espíndola *et al.* 2017) have primarily used PRF, while SRF have not, despite they provide information on properties of the lower crust and Moho depth. Stacking PRF (Zhu & Kanamori 2000) is a frequently used methodology to estimate the crustal thickness. This procedure sums up the amplitudes of the primarily converted *Ps* waves, along with its multiples, to obtain the thickness H and the *P*- and *S*-wave velocity ratio, $\frac{V_P}{V_S}$, of the crust. We decided to stack SRF together with PRF to add information from the primarily *Sp* conversion at each discontinuity, constraining the thickness estimation of each layer, mainly the deeper layers that could be masked by *Ps* multiples from midcrust discontinuities.

2 DATA AND RECEIVER FUNCTION PRODUCTION

2.1 Data

We used 159 broad-band stations (Fig. 1 and Table S1) that are part of three permanent seismic networks and five temporary arrays within Guerrero, Oaxaca, Puebla and Veracruz: The broad-band network of the Servicio Sismológico Nacional (SSN, National Seismological Service, Pérez-Campos *et al.* 2018; SSN 2018); the Veracruz Seismic Network (UV; Córdoba-Montiel *et al.* 2018); the Oaxaca

Network (OxNet; Cabral-Cano *et al.* 2018); the National Disaster Prevention Center (CENAPRED); Tuxtepec station (TUXT) belonging to the Veracruz-Oaxaca experiment (VEOX; VEOX 2010; Melgar & Pérez Campos 2011); the Los Humeros Network (HUM); the Geometry of Cocos array (GECO) and the MesoAmerican Subduction Experiment (MASE; MASE 2007; Pérez-Campos *et al.* 2008).

Broad-band data from the permanent SSN network covers a time span since 2012 for all stations, except for HUIG, OXIG, PNIG and TPIG, which have continuous data available since 2002, and stations HLIG and TLIG since 2009. Data from UV covers 2014 and 2015 and data from station POCC of CENAPRED, only covers 2013. The temporary array OxNet data set is available since mid-2006 to early 2012; station TUXT operated for 2 yr, from August 2007 to August 2010; data available from Los Humeros network spans from September 2011 to August 2012 and only five events were recorded during this period; GECO network was deployed as a moving array from 2013 to mid-2018, each station recorded approximately 1 yr; data from MASE is available from 2005 to 2007; and VEOX from 2007 to 2009 (Fig. 2).

We use teleseismic earthquakes at epicentral distances ranging from 30° to 90° for PRF, and 65° to 85° for SRF, and with magnitudes $M_w \geq 6.0$ (Fig. 3). Permanent networks registered considerably more events in comparison with the temporary arrays, given the time span of operation (Fig. 2). For some stations of the SSN network, catalogues included more than 600 events. For this reason, we implemented a methodology to automatically select the phases onsets.

2.2 Receiver function production

Manual phase picking limited the number of events that we could analysed to those with high signal to noise ratio, SNR. However, we wanted as many RFs as possible for stations that operated only for a short period; on the other hand, we had to deal with many events for the permanent stations. These two situations motivated the implementation of an automatic phase-picking algorithm, APPA.

We implemented the algorithm by Saragiotis *et al.* (2000; 2002) based on the kurtosis characteristic function (KCF), originally designed for local earthquakes, to detect the phase onset. The kurtosis is a high-order statistic that measures the shape of a statistical distribution. Seismic noise would be represented by a Gaussian distribution. On the other hand, a non-Gaussian distribution would be attributed to the onset of a seismic wave within the data (Saragiotis *et al.* 2000). The transition, from Gaussian to non-Gaussian distribution, aids to identify the beginning of a seismic event (Saragiotis *et al.* 2002). We follow Baillard *et al.* (2014) corrections to the KCF to select the onset of the phase accurately rather than the peak value of the wave.

To test the effects of a bias on the picking result of our APPA on the estimated RF, we selected a seismogram from station IXJU where the *P* wave was clearly identified, and we shifted this phase selection by ±50, ±25, ±15, ±10, ±5, ±2.5, ±1.0, ±0.5 and ±0.1 s. We then produced the corresponding RF. Fig. 4 shows the RF computed for each shift (blue solid line). This is compared with the RF obtained from the signals which phases were carefully manually picked (dashed red line). To measure the waveform similarity between the RFs, produced by manual picking and the ones shifted, we compute the correlation coefficient. From this analysis, we notice that shifts between ±15 s produce RF at least 80 per cent similar. We obtained similar results for SRF.

Based on the correlation coefficient, we establish an acceptance criterion. We first calculate the time difference (Δt) of the detected wave onset time, t_K, by the APPA between pairs of components (vertical with north–south; vertical with east–west; and north–south with east–west). If the difference for all pairs were less than 15 s, we then accept t_K of the vertical component. Otherwise, we compare t_K with the theoretical phase arrival calculated with TauP (Crotwell & Owens 1999), assuming the 1-D velocity model IASP91 by Kennett (1991), t_T. If this difference also exceeds 15 s, we then use t_T.

In case that both comparisons, between components and with theoretical arrival, exceed 15 s, the event is rejected from automatic phase picking. The implemented APPA for the teleseismic records might be somehow insensitive in terms of selecting the onset of the phase if the SNR is not high enough to distinguish the arrivals. In that case, the rejected signals are moved for manual selection and once the phases are manually picked, they are incorporated into the process of obtaining the RFs.

To equalize *P*- and *S*-wave RF, we cut the signal in a 120 s window, 30 s before and 90 s after the *P*-wave arrival and 90 s before and 30 s after the *S* wave. We then rotate the geographical components (north–south, east–west and vertical) to a Vertical-Radial-Transverse (ZRT) system; and perform a second rotation to a Longitudinal-Radial-Transverse (LQT) system to maximize the *P*-wave energy on the longitudinal component for the PRF and to minimize the *P*-wave energy on the same component for the SRF (Sodoudi *et al.* 2006). We then deconvolve the longitudinal from the radial components to get PRF, and the radial from the longitudinal components to get SRF. We follow the methodology proposed by Langston (1979), Ammon (1991) and Ligorría & Ammon (1999) for PRF, and adapted by Sodoudi *et al.* (2006) for SRF.

2.3 Automated complementary ensemble empirical mode decomposition

Prior to analysing the RFs, we process each RF with an empirical mode decomposition (EMD) algorithm (Huang *et al.* 1998) adapted and automated by Montealegre-Cázares & Pérez-Campos (2016) to enhance the coherency of the pulses associated with discontinuities within the crust, such as the base of a sedimentary layer, the boundary between the upper and lower crust and the Moho.

EMD is an adaptive algorithm to analyse non-linear signals describing non-stationary and non-periodical phenomena (Huang *et al.* 1998). The EMD decomposes the main signal into several Intrinsic Mode Functions (IMFs) which have spectral energy in different restricted frequency bandwidths. An original time series, decomposed by the EMD, could be represented as:

$$X(t) = \sum_{i=1}^{n} c_i + r_n, \tag{1}$$

where $X(t)$ is the original signal, c_i are the computed IMFs and r_n is the residual. Numerical problems, known as mode mixing, where remnant energy from some IMFs is observed in another IMF, are corrected following the methodology proposed by Wu & Huang (2009) and Yeh *et al.* (2010), by adding white noise (positive and negative, scaled amplitude) while the decomposition is being performed. They named the algorithm Complementary Ensemble Empirical Mode Decomposition (CompEEMD). Furthermore, Montealegre-Cázares & Pérez-Campos (2016) modified the algorithm to automatically constrain the CompEEMD parameters to decompose large amount of data without human intervention. They named the algorithm Automated and Complementary Ensemble

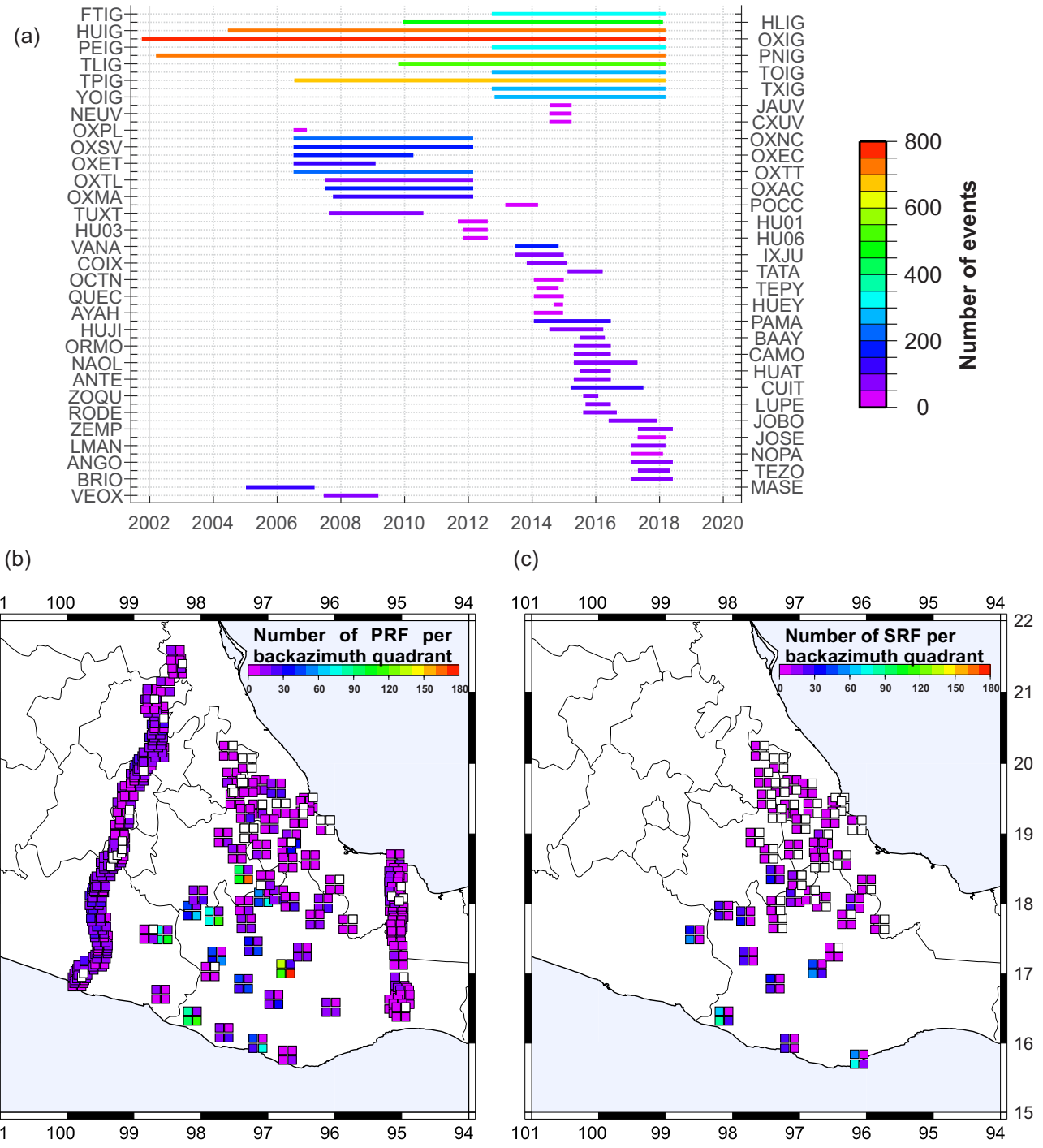

Figure 2. (a) Time coverage and number of events per station. The length of each coloured line shows the time period when the station operated (temporal stations) or the period of the catalogue used (permanent stations). The colour assigned to the line shows the numbers of events used to compute the RFs. (b) Number of PRF computed for each station at each 90° quadrant. (c) Numbers of SRF per station and 90° quadrant. White squares on (b) and (c) denote a lack of RFs on that backazimuth.

Empirical Mode Decomposition (ACompEEMD). Further details can be found in the Supplementary Material 2.

Fig. 5 shows a set of decomposed RFs at station TUXT. Different IMFs or a combination of IMFs enhance the coherency of pulses associated with distinct seismic discontinuities. The first three IMFs largely improve the continuity of pulses associated with interfaces within the crust. The first component (IMF 1, Fig. 5b) improves visualization and continuity of the pulse related to shallower discontinuities within the crust (coloured pulses seen before 1 s). IMF 2 and the combination of IMF 2 and 3 (Figs 5c and d, respectively) enhance the converted *Ps* wave coming from mid-crust and Moho discontinuities (pulses observed around 2 and 4.5 s).

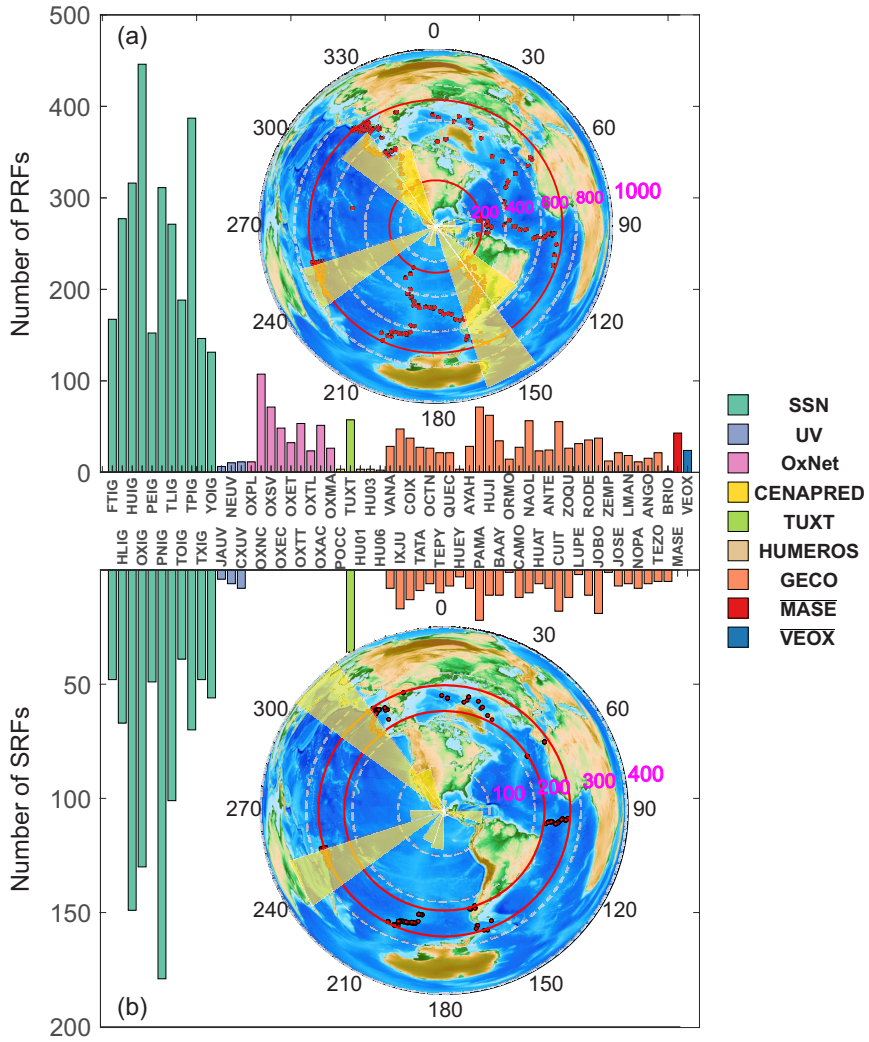

Figure 3. Total number of RF per station and geographical distribution of events (red dots). The yellow rose diagram shows the backazimuth distribution of events. Numbers in magenta and grey dashed circles display the number of events per backazimuth. The red circles delimit epicentral distances from 30° to 90° for (a) PRF, and from 65° to 85° for (b) SRF. (a) Events used to obtain PRFs and number of PRFs per station. For MASE and VEOX stations, the bar shows the average PRFs for the stations. (b) Events used to obtain SRFs and number of SRFs per station.

3 RECEIVER FUNCTION ANALYSIS

To determine the thickness of the crust, we estimate the depth of the Mohorovičić discontinuity (Moho) by stacking the RF amplitudes and transform them into the thickness-V_P/V_S (H–κ) domain. We modified the methodology by Zhu & Kanamori (2000) to include SRF information, and to do it sequentially for three layers.

3.1 H–κ azimuthal analysis

Zhu & Kanamori (2000) developed a methodology where the traveltimes and amplitudes of the converted phases *Ps*, *PpPs* and *PsPs* + *PpSs*, are mapped into the H–κ space, H is the thickness of the layer and κ, the V_P/V_S ratio, where $V_P$and V_S are *P*- and *S*-wave velocities, respectively. To stack the amplitudes in the H–κ domain, Zhu & Kanamori (2000) defined the transforming equation as:

$$A_P(H,\kappa) = w_1 r(t_1) + w_2 r(t_2) - w_3 r(t_3), \quad (2)$$

where $A_P(H,\kappa)$ is the stacking function; $r(t_i)$, the amplitudes of the converted phases at the predicted times t_i, and w_i, the weighting factors which sum to 1, where $w_1 = 0.7$, $w_2 = 0.2$ and $w_3 = 0.1$. To include the SRF data, we added the *Sp* conversion into the H–κ domain as

$$A_S(H,\kappa) = r(t_4), \quad (3)$$

and we used the joint transforming equation defined by

$$A_{PS}(H,\kappa) = w_1' A_P(H,\kappa) + w_2' A_S(H,\kappa), \quad (4)$$

where w_j' are weighting factors, arbitrarily chosen and tested on a model of three layers of 10 km each, that sum to 1, where $w_1' = 0.7$ and $w_2' = 0.3$.

Since the converted-phases incidence angles are not vertical, the conversion point is projected on the discontinuity surface, at a horizontal distance that depends on the depth of the discontinuity and the ray parameter. Furthermore, since the layers might not have a constant thickness, the horizontal distance to the conversion point might vary depending on the backazimuth. We estimate this horizontal distance, and therefore the crustal thickness, by means of a weighted model according to the number of PRF and SRF.

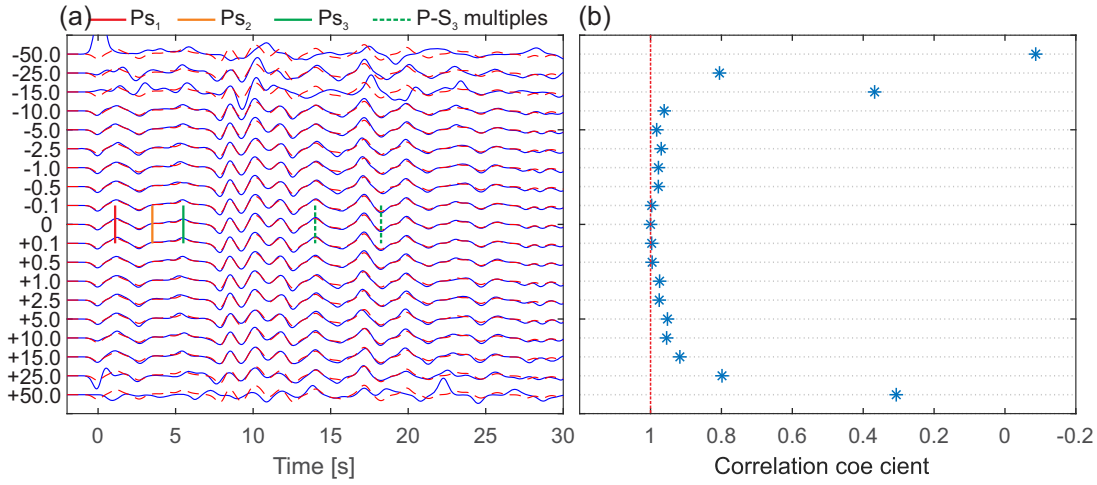

Figure 4. (a) Comparison of receiver functions (RFs), from station IXJU, generated from signals with a shift of the picked phase arrival (continuous blue line) with the RF obtained from signals with a carefully manual pick for the *P* arrival (discontinuous red line, signal 0). The RFs are ordered by the applied time shift, indicated in the vertical left axis; negative times (e.g. −50.0) imply the phase arrives *n* seconds earlier than the original. Positive times imply the phase arrival is *n* seconds later than the original. (b) Correlation coefficient between the RFs that result from the shifted signals and the original RF.

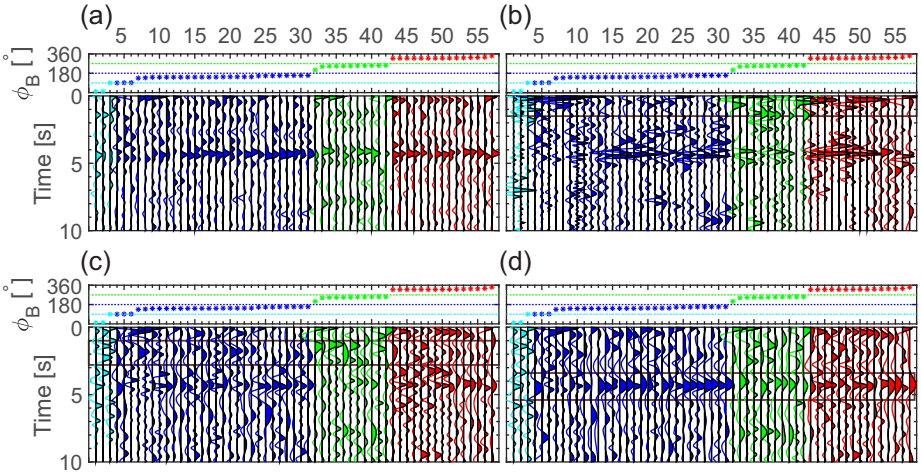

Figure 5. Receiver functions for station TUXT. They are ordered by backazimuth. The colour corresponds to their azimuthal group. (b) IMF1 of all RFs. Pulses before 2 s, enclosed by the box, are enhanced. (c) IMF2 of all RFs. Pulses at ∼2 s, enclosed by the box, are enhanced. (d) Combination of IMF2 + IMF3. This combination enhances the pulse between 4 and 5 s, enclosed by the box.

We group the RFs at each station in four backazimuth subsets (group 1: 0–90°, group 2: 90–180°, group 3: 180–270°, group 4: 270–360°). We choose these intervals given the distribution of backazimuths of the teleseisms employed to obtain the RFs (Fig. 3) To determine the backazimuth, ϕ, and the attributed distance, d, we compute weighting factors w_P = NPRF/NTRF and w_S = NSRF/NTRF. NPRF, NSRF and NTRF are the number of PRF, the number of SRF, and the total number of RF, respectively (i.e. NTRF = NPRF + NSRF).

(1) If there is a major contribution from PRF, $w_p > w_s$, and

$$d = d_{Ps} + w_S d_{Sp}. \quad (5)$$

(2) If there is a major contribution from SRF,

$$d = d_{Sp} + w_P d_{Ps} \quad (6)$$

(3) The backazimuth is computed as:

$$\phi = \bar{\phi}_P w_P + \bar{\phi}_S w_S, \quad (7)$$

where $\bar{\phi}_P$ and $\bar{\phi}_S$ are, respectively, the mean of the backazimuth for the PRF and the SRF obtained at each station. Then, we estimate the thickness of the layer, H, using eq. (5) and (6) and attribute it to a distance d with a backazimuth Φ from the position of the station. Fig. 6 shows a schematic diagram of the procedure. Panels in a) show a model of a horizontal layer over a half-space. Left-hand panel shows the ray paths for *P* and *S* waves, in blue and red arrows, respectively, and its conversions at the interface at a depth *H*. d_{Ps} and d_{Sp} are the horizontal distances of the pierce points of *Ps* and *Sp*, respectively. The location of the attributed conversion point depends on the weighting factors w_P and w_s. Central panel shows four different types of contribution. The colour of the circle represents the depth of the discontinuity. For a horizontal layer over a half-space:

(1) There is no azimuthal variation of the depth, therefore,
(2) Circles from any direction are the same colour and the,
(3) Horizontal distance depends only on the weighting factors computed from the number of PRF and SRF.

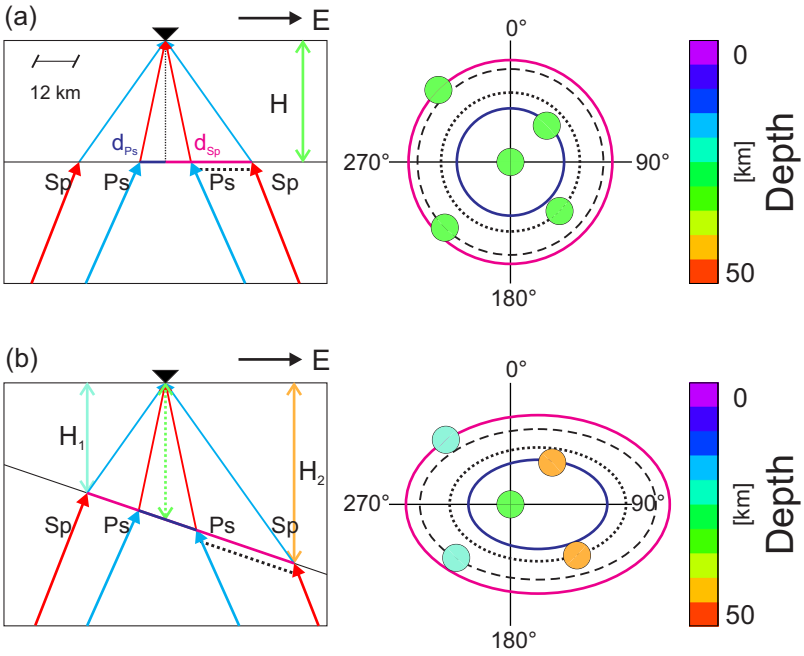

Figure 6. Conversion point determination. The raypaths for *P* and *S* waves are shown in blue and red arrows, respectively, converted at the interface at a depth *H*. d_{Ps} and d_{Sp} are the horizontal distances. (a) Model of a horizontal layer over a half-space (left). Central panel shows four different contributions according to the number of PRF and SRF. The circle colour represents the depth to the discontinuity. For this model we assume *H* to be approximately 35 km. Detailed description of the diagram is explained in section 3.1. (b) Model of a dipping layer over a half-space. For this model, the depth of the discontinuity depends on the arrival direction of the incoming wave. Conversions at the updip section of the discontinuity map a thinner upper layer than those at the downdip section of the layer, which is represented by the colour of the circle. Horizontal distances are computed in the same manner as in Fig. 5(a) and fully detailed in Section 3.1.

If there is contribution:

(1) From only PRF, the green circle, showed between 0° and 90°, is placed over the dark blue circumference. If,
(2) There are more PRF, showed between 90° and 180°, the circle is placed at a distance closer to d_{Ps}, along the dotted circumference. On the other hand, if
(3) There are more SRF, showed between 180° and 270°, the circle is placed at a distance closer to d_{Sp}, over the dashed circumference. The last case is if
(4) There are only SRF, showed between 270° and 360°, in which case the circle is placed over the magenta circumference.

In the figure the green colour represents approximately 35 km depth, assuming $d_{Ps} = H/3$, the horizontal distance is ∼12 km. Lower panels, Fig. 6(b), represent a dipping layer over a half-space model. Raypaths and horizontal distances are colour coded as in Fig. 6(a). For this model, the depth to a discontinuity depends on the direction of arrival and it is represented by the colour of the circle. For the model shown in Fig. 6(b), on the left-hand panel, waves arriving from the west are converted at the updip section of the discontinuity, whereas waves coming from the east are converted at the downdip section of the discontinuity. The horizontal distances are computed in the same manner than those in Fig. 6(a). Central panel in Fig. 6(b) represents the four cases of contribution of PRF and SRF, to compute the horizontal distance from the station to the conversion point for a dipping layer. Therefore, for each station, we will have four depth estimations for each crustal seismic discontinuity, or less if no RF was obtained for a backazimuth group.

The uncertainty for H is computed for each layer following Persaud *et al.* (2007), by bootstrapping (100 samples) the RFs to obtain the distribution of the estimator $\hat{H}$ and select percentiles 5, 50 and 95, which define our estimated thickness and their confidence intervals, H_{50} [H_5, H_{95}].

3.2 Sequential procedure

Yeck *et al.* (2013) showed that without accounting for a low velocity sedimentary basin the Moho depth could be mischaracterized by ∼10 km. To avoid overestimation of crustal thickness we modified the methodology proposed by Zhu & Kanamori (2000) and Yeck *et al.* (2013) to consider, as a sum of a three-layer model, the effect of upper low velocity layers.

We first compute the thickness of the uppermost layer following Zhu & Kanamori (2000) and apply a moveout correction to the RF as proposed by Gurrola *et al.* (1994). We then compute the bottom of the second layer, where the thickness of the first layer is considered to sum up the two-layer model, and once again, the moveout is corrected from the base of the first layer to the end. This procedure is repeated for the three-layer model, to add up the entire crustal thickness. Layer 1 goes from the surface to the base of the sedimentary layer, Layer 2 initiates from the base of the first layer and goes to the mid-crust discontinuity, and Layer 3, from mid-crust to Moho discontinuity. Initial *Vp* values used (4.45, 5.35 and 6.925 km s^{-1} for layers 1–3, respectively) were based on the Oaxaca regional model from Valdés *et al.* (1986).

4 RESULTS

We determined the thickness of the crustal layers, referred to the surface, which include the bottom of a sedimentary layer (Fig. 7a),

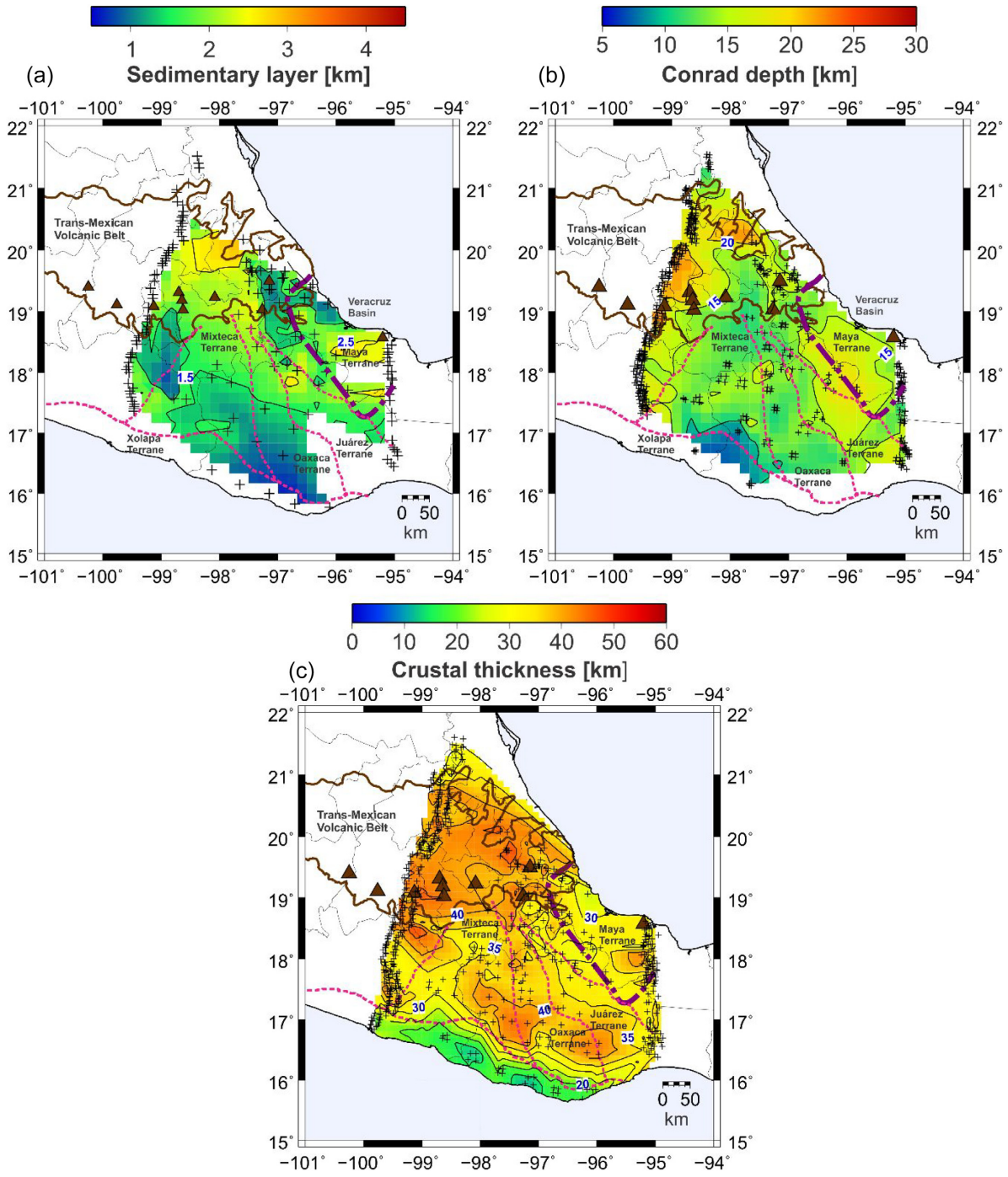

Figure 7. (a) Topography of the crustal discontinuities in the study area. Dashed lines in magenta, delineate the boundaries from major tectonostratigraphic terranes in south-central Mexico. The Veracruz basin is delineated with a dash–dotted purple line; and the Trans-Mexican Volcanic Belt with a solid brown line. (a) Depth to the base of a shallow low-velocity layer. (b) Depth to Conrad discontinuity. (c) Crustal thickness.

the Conrad discontinuity (Fig. 7b), and the Moho (Fig. 7c) by interpolating, with Generic Mapping Tools (GMT, Wessel & Smith 1998), the estimated depth for each group of RFs per station. The performed azimuthal analysis was employed to detect any possible change in crustal thickness that could be correlated to the different terranes found in south-central Mexico. Theoretically, RFs created with a high-frequency Gaussian pulse width of 0.75 s (Gaussian filter parameter $a = 5$) can resolver layers of 0.9 km. Our RFs were obtained with this value. Therefore, they can resolve, at least, a 1 km layer.

The first discontinuity ranges from 1–4 km depth with a mean value of ∼2 km and it is associated, for most of the study area, with the bottom of the sedimentary layer. A second discontinuity is shown in Fig. 7(b), its depth is of a few kilometers (< 5 km) near the Pacific coast, and deeper (∼20 km) below the Mixteca, Oaxaca and Juárez terranes and the TMVB. The third discontinuity, the depth to

the Moho (crustal thickness), is shown in Fig. 7(c). Close to the Pacific coast (Xolapa terrane), we observe a thin crust of 15 ± 1.0 km. In the middle section of our study area (Mixteca, Oaxaca, and Juarez terranes), the thickness of the crust is approximately 40 km. In central Oaxaca (Mixteca, Oaxaca, and Juarez terranes) and the TMVB, we observed a thicker crust ranging between 30 and 50 ± 2.0 km. Along the coastal plain of the Gulf of Mexico we observe a crustal thickness of ∼30 ± 1.6 km.

Our results, summarized in Table 1, can be divided into four groups: (1) a thin crust (16.2 ± 0.9 km); observed at the southwestern edge of the Xolapa terrane with a thin sedimentary layer (1.6 ± 0.1 km) and a shallow Conrad discontinuity (7.4 ± 0.5 km); (2) the coastal plain of the Gulf of Mexico with an intermediate thick crust (31.6 ± 1.6 km), with a slightly thicker sedimentary layer (1.8 ± 0.1 km) and a deeper Conrad discontinuity (15.2 ± 0.9 km); (3) a thicker crust (41.2 ± 2.0 km), identified at the eastern edge of the TMVB, with the thickest sedimentary layer (2.0 ± 0.1 km), aligned with the eastern most volcanic chain within the TMVB, and an intermediate depth Conrad discontinuity (15.5 ± 2.1 km), (4) and central thicker crust (37.0 ± 1.9 km) with thick sedimentary layer (1.8 ± 0.1 km), beneath the Oaxaca terrane, and the Conrad discontinuity (12.6 ± 0.7 km) closely following the Moho topography.

5 DISCUSSION

5.1 Upper-crustal discontinuity

Even though it does not correlate with the terranes, a presumably thicker sedimentary layer is located along the west margin of the Veracruz sedimentary basin (west to the Maya terrane). This is also true of a basin in central Oaxaca which lies in the hanging wall of the Oaxaca fault, a major Cenozoic normal fault system with a north–south average direction (Álvarez *et al.* 1994), almost covering the entire Oaxaca terrane. Beneath the Pico de Orizaba volcano we observe the largest thickness, which is probably not a sedimentary layer but a deeper discontinuity that is part of the volcanic structure.

5.2 Conrad discontinuity

The estimated depth of ∼15 km for the upper/lower interface agrees well with the depth observed on Guerrero (Iglesias *et al.* 2001) and Oaxaca (Valdés *et al.* 1986) identified as the Conrad discontinuity (Litak & Brown 1989).

5.3 Moho discontinuity

Close to the Pacific coast (Xolapa terrane) we observe a thin crust of 15 ± 1.0 km, which is 5 km thicker than the thickness estimated by Valdes *et al.* (1986), and 5 km thinner in comparison with the observed thickness of Nava *et al.* (1988). In some cases, a subducting plate may erode the overriding plate (Stern 2011). In south-central Mexico, the Cocos plate subducts beneath the North American plate and subduction erosion may be responsible for the thinned crust observed along the Xolapa terrane (Morán-Zenteno *et al.* 1996).

On the other side of the country, we identify a slight crust thinning of approximately 6 km, from 37 ± 1.9 km in central Oaxaca to 31.6 ± 1.9 km towards the Gulf of Mexico, beneath the Veracruz basin (Maya terrane). Rifting processes that caused the opening of the Gulf of Mexico during the Mesozoic (Marton & Bluffer 1994) gave rise to a stretched crust, which could explain our observed thinned crust beneath the Gulf of Mexico coastal plain.

Beneath central Oaxaca (Mixteca, Oaxaca, and Juarez terranes) and the TMVB, we observed a thicker crust ranging between 30 and 50 ± 2.0 km, which is in the range observed by Valdés *et al.* (1986) and Iglesias *et al.* (2001).

Estimations of crustal thickness in Oaxaca by Espíndola *et al.* (2017) are directly compared with our results due to the similarity of the processes. However, their results seem to overestimate the crustal thickness. For station PNIG they obtained a Moho depth of 24.1 ± 6.0 km against our preliminary uncorrected Moho of 24.8 [22.9, 25.0] km and once corrected we got 13.0 [12.1, 13.5] km; for station OXIG they obtained a Moho depth 41.8 ± 6.3 km against our uncorrected Moho of 35.6 [36.8, 37.1] km and for a three-layer model, including a sedimentary layer, we got 38.6 [38.0, 39.6], however, in comparison with the estimation for a layer over a half-space, the three layer model is ∼3 km thicker. OXIG station presents a large azimuthal variation of the expected pulse, converted at the Moho, which could affect the preliminary estimation if early arrivals had a bigger contribution to the stacking procedure. Finally, for station TPIG they obtained 42.0 ± 2.3 km, against our Moho depth of 42.3 [41.6, 42.9] km for a three-layer model. We suggest these differences rely on the corrections we make for the upper layers which delay the converted phases leading to an overestimation of the crustal thickness (Yeck *et al.* 2013) if this shallow layer is not considered, mainly the upper-most low-velocity layer.

The, relatively similar, crustal thickness over central Oaxaca agrees with Jording *et al.* (2000) who do not observe any boundary at depth between Oaxaca and Juarez terrane from magnetotelluric (MT) transfer function data, suggesting that these terranes could share a similar basement. On this matter, we observe differences between the middle section (Mixteca, Oaxaca and Juarez terranes) and the south section (the Xolapa terrane), and slightly different in comparison with the east section (Veracruz basin) and beneath the northern section (TMVB).

Azimuthal anisotropy vectors computed by Castellanos *et al.* (2018), are plotted in Fig. 8 (upper panel). In the southernmost region where we observe the thinnest crust, along the Xolapa terrane, the fast direction is trench parallel suggesting that anisotropy in the upper crust may be dominated by fractures produced by lateral compression (Castellanos *et al.* 2018). Furthermore, the azimuthal effects on a RF from anisotropic, horizontal layer, would shift the arrival of the direct *P*-wave on the radial component and the amplitude of *Ps* conversion would vary in all directions, with maximum amplitude on the direction of the fast axis of anisotropy and with minimum amplitude at 180° (Tian *et al.* 2008). However, measurements and the effect of crustal anisotropy on RFs is out of reach of this paper.

In general agreement with Castellanos *et al.* (2018), our crustal thickness measurements indicate a possible isostatically overcompensated region over the Veracruz basin, where we would not expect a largely thinned crust above sea level according to the Airy model. In contrast, the central region of our study appears to be isostatically compensated, which is also supported by Urrutia-Fucugauchi & Flores-Ruiz (1996) from studying gravity data in that region.

Arzate-Flores *et al.* (2016) observed, along a magnetotelluric profile in Oaxaca, an anomalous conductivity zone (Fig. 8, lower panel) near 25 km depth, close to the coast. They suggest it originated from water expelled from closing fractures and pores at the top of the subducting Cocos plate along the seismic coupling region. This anomaly agrees with our proposed depth of the Moho

Table 1. Depth to discontinuities within the crust for a three-layer media and for four regional divisions.

Group	Layer	Depth [km]	Terrane
(1) South-western Mexico	Sedimentary	1.6 ± 0.1	Xolapa
	Conrad	7.4 ± 0.5	Xolapa
	Crust	16.2 ± 0.9	Xolapa
(2) Gulf of Mexico coastal plain	Sedimentary	1.8 ± 0.1	Maya
	Conrad	15.2 ± 0.9	Maya
	Crust	31.6 ± 1.6	Maya
(3) Trans-Mexican Volcanic Belt	Upper-most volcanic	2.0 ± 0.1	TMVB
	Conrad	15.5 ± 2.1	TMVB
	Crust	41.2 ± 2.0	TMVB
(4) Central Oaxaca	Sedimentary	1.8 ± 0.1	Oaxaca, Mixteca
	Conrad	15.5 ± 2.1	Oaxaca, Mixteca
	Crust	41.2 ± 2.0	Oaxaca, Mixteca

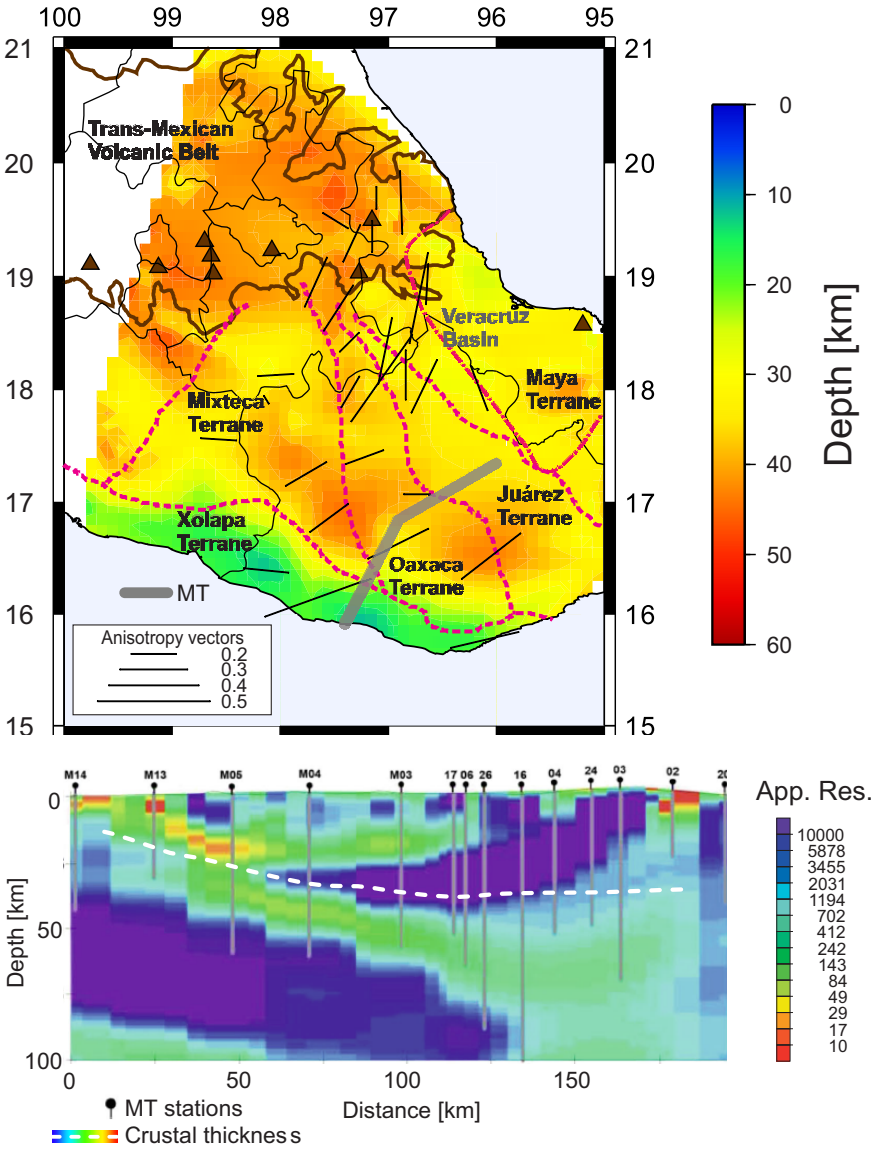

Figure 8. Top panel: crustal thickness. Bold black lines show the azimuthal anisotropy vectors from Castellanos *et al.* (2018). Bold grey line shows the MT profile from Arzate-Flores *et al.* (2016). Bottom panel: resistivity model along the magnetotelluric profile modified from Arzate-Flores *et al.* (2016). Dashed white line delineates the crustal thickness proposed in this study along the same profile.

up to 50 km from the coast. Then, between 75 and 150 km inland, our Moho depth (∼35 km) is slightly shallower than the 40–50 km observed by Arzate-Flores *et al.* (2016). They observe a high resistivity region, which they suggest it might be associated with a dry and colder basement of the Oaxaca terrane.

6 CONCLUSIONS

Our results for crustal thickness agree well with previous studies. However, thanks to our network coverage, we studied in detail a broad area in south-central Mexico, by estimating the depth of three seismic interfaces: the bottom of a low velocity layer, mainly associated with the base of sedimentary basins; the Conrad discontinuity; and the Mohorövičić discontinuity.

The sedimentary layer (Fig. 7a) is found mostly along all the study area. Conrad discontinuity (Fig. 7b) closely follows the geometry of the crustal thickness. Fig. 7(c) shows the spatial correlation between crustal thickness and the different terranes. Crustal thickness along Mixteca, Oaxaca and Juarez terranes seem similar, however, they differ from those under the TMVB, Xolapa and Maya terranes. For the last two, we find an eroded and stretched thinned crust, respectively.

Our results, summarized in Table 1, show that crustal thickness is closely correlated with the different terranes and can be divided into four groups: (1) a thin crust (16.2 ± 0.9 km); observed at the southwestern edge of the Xolapa terrane with a thin sedimentary layer (1.6 ± 0.1 km) and a shallow Conrad discontinuity (7.4 ± 0.5 km); (2) the coastal plain of the Gulf of Mexico with an intermediate thick crust (31.6 ± 1.6 km), with a slightly thicker sedimentary layer (1.8 ± 0.1 km) and a deeper Conrad discontinuity (15.2 ± 0.9 km); (3) and a thicker crust (41.2 ± 2.0 km), identified at the eastern edge of the TMVB, with a thick upper-most layer (2.0 ± 0.1 km), aligned with the eastern most volcanic chain within the TMVB, and intermediate depth Conrad discontinuity (15.5 ± 2.1 km) and (4) central thicker crust (37.0 ± 1.9 km) with thick sedimentary layer (1.8 ± 0.1 km), beneath the Oaxaca terrane, and a Conrad discontinuity (12.6 ± 0.7 km) closely following the crustal thickness topography.

The proposed model of the crust in south-central Mexico, would be beneficial to reduce the uncertainty of depth estimation for regional earthquakes; also, the crustal model will help addressing other important tectonic unknowns, such as the possible presence of a slab tear in the same region (e.g. Fasola *et al.* 2016; Castellanos *et al.* 2018); and the crustal variations beneath the TMVB encourages tomography studies to delineate low-velocity anomalies associated with magmatic processes in the region.

DATA AND RESOURCES

Broad-band data from the permanent SSN and UV networks is available by request http://www.ssn.unam.mx/doi/networks/mx/). Data from station POCC of CENAPRED should be requested to Ing. Gilberto Pescina (gilberto@cenapred.unam.mx). Data from OxNet is available since mid-2006 to early 2012 at http://tlalocnet.udg.mx/. Data from MASE and VEOX experiments are available from the IRIS Data Management Center, http://service.iris.edu/fdsnws/dataselect/1/. Data from Los Humeros network should be requested to Instituto de Ingeniería, UNAM (www.iingen.unam.mx/, JLermoS@iingen.unam.mx); data from GECO network can be requested to PI X. Pérez-Campos (xyoli@igeofisica.unam.mx) and will be open on 2021. Topography grids were provided by Amante & Eakins (2009).

ACKNOWLEDGEMENTS

This work was supported by Universidad Nacional Autónoma de Mexico through project UNAM-PAPIIT IN105816, and Consejo Nacional de Ciencia y Tecnología (Conacyt) through project 177676. SSN data was obtained by the Servicio Sismológico Nacional (México), station maintenance, data acquisition and distribution are possible thanks to its personnel. This work is also partly based on seismic data generated from OxNet through an NSF Grant EAR-1246944 to M. Brudzinzki. We thank the personnel involved in operation and maintenance of all the stations used in this work. We especially thank Antonio de Jesús Mendoza Carvajal (SSN), and Jorge Real Pérez (Instituto de Geofísica, UNAM) for installing and maintaining the GECO stations and Oscar Díaz-Molina and Luis Salazar-Tlaczani (Instituto de Geofísica, UNAM) for the OxNet operations. We also thank Francisco Córdoba-Montiel (UV), Javier Lermo-Samaniego (Los Humeros) and Gilberto Castelán-Pescina (CENAPRED) for providing data used on this project. We thank the Academic Writing UNAM-Canada program for their assistance in the elaboration of this paper. M. Rodríguez-Domínguez had a Conacyt graduate scholarship. Figs 1, 2 and 6 were made using the Generic Mapping Tools version 4.5.9 (www.soest.hawaii.edu/gmt; Wessel & Smith 1998). Finally, we thank the editor Prof Frederik Simons, Dr Luca Ferrari and an anonymous reviewer for their valuable comments that improved this paper.

REFERENCES

Álvarez, S.A.A., Gutiérrez, F.O. & Samaniego, Á.F.N., 1994. Structural evolution of the Sierra de Juarez mylonitic complex, State of Oaxaca, Mexico. *Rev. Mex. Cienc. Geol.,* **11**(2), 3.

Amante, C. & Eakins, B.W., 2009. ETOPO1 1 arc-minute global relief model: procedures, data sources and analysis. *NOAA Technical Memorandum NESDIS NGDC-24. National Geophysical Data Center, NOAA.* doi:10.7289/V5C8276M [22/04/2015].

Ammon, C.J., 1991. The isolation of receiver effects from teleseismic P waveforms. *Bull. seism. Soc. Am.,* **81**(6), 2504–2510.

Ammon, C.J. & Zandt, G., 1993. Receiver structure beneath the southern Mojave block, California. *Bull. seism. Soc. Am.,* **83**(3), 737–755.

Arzate-Flores, J.A., Molina-Garza, R., Corbo-Camargo, F. & Márquez-Ramírez, V., 2016. Low angle contact between the Oaxaca and Juárez terranes deduced from magnetotelluric data, in *Geodynamics of the Latin American Pacific Margin,* pp. 3357–3371, eds ,Bandy, W.L., DAÑOBEITIA, J., Gutiérrez, C., Taran, Y., Bartolomé, R., Springer.

Baillard, C., Crawford, W.C., Ballu, V., Hibert, C. & Mangeney, A., 2014. An automatic kurtosis-based P- and S-phase picker designed for local seismic networks. *Bull. seism. Soc. Am.,* **104**(1), 394–409.

Cabral-Cano, E. *et al.*, 2018. TLALOCNet: a continuous GPS-Met backbone in Mexico for seismotectonic and atmospheric research. *Seismol. Res. Lett.,* **89**(2A), 373–381.

Castellanos, J.C., Clayton, R.W. & Pérez-Campos, X., 2018. Imaging the eastern Trans-Mexican Volcanic Belt with ambient seismic noise: evidence for a slab tear. *J. geophys. Res.: Solid Earth,* **123**(9), 7741–7759.

Chen, Y., Niu, F., Liu, R., Huang, Z., Tkalčić, H., Sun, L. & Chan, W., 2010. Crustal structure beneath China from receiver function analysis. *J. geophys. Res.,* **115**(B3), 1–22.

Córdoba-Montiel, F., Iglesias, A., Pérez-Campos, X., Sieron, K., De Trabajo del Servicio Sismológico Nacional, G., Valdés-González, C., Singh, S.K. & Pacheco, J.F., 2018. The broadband seismological network of Veracruz, Mexico: toward a regional seismotectonic interpretation. *Seismol. Res. Lett.,* **89**(2A), 345–355.

Crotwell, H.P. & Owens, T.J., 1999. The TauP toolkit: flexible seismic travel-time and raypath utilities. *Seismol. Res. Lett.,* **70**(2), 154–160.

Espíndola, V.H., Quintanar, L. & Espíndola, J.M., 2017. Crustal structure beneath Mexico from receiver functions. *Bull. seism. Soc. Am.,* **107**(5), 2427–2442.

Farra, V. & Vinnik, L., 2000. Upper mantle stratification by P and S receiver functions. *Geophys. J. Int.,* **141**(3), 699–712.

Fasola, S. *et al.*, 2016. New perspective on the transition from flat to steeper subduction in Oaxaca, Mexico, based on seismicity, nonvolcanic tremor, and slow slip. *J. geophys. Res.: Solid Earth,* **121**(3), 1835–1848.

Ferrari, L., Orozco-Esquivel, T., Manea, V. & Manea, M. 2012. The dynamic history of the Trans-Mexican Volcanic Belt and the Mexico subduction zone. *Tectonophysics,* **522,** 122–149.

Gaite, B., Iglesias, A., Villaseñor, A., Herraiz, M. & Pacheco, J.F., 2012. Crustal structure of Mexico and surrounding regions from seismic ambient noise tomography. *Geophys. J. Int.,* **188**(3), 1413–1424.

Gurrola, H., Minster, J.B. & Owens, T., 1994. The use of velocity spectrum for stacking receiver functions and imaging upper mantle discontinuities. *Geophys. J. Int.,* **117**(2), 427–440.

Huang, N.E. *et al.*, 1998. The empirical mode decomposition and the Hilbert spectrum for nonlinear and non-stationary time series analysis. *Proc. Roy. Soc. Lond., A Math. Phys. Eng. Sci.,* **454**(1971), 903–995.

Iglesias, A., Cruz-Atienza, V.M., Shapiro, N.M., Singh, S.K. & Pacheco, J.F., 2001. Crustal structure of south-central Mexico estimated from the inversion of surface-wave dispersion curves using genetic and simulated annealing algorithms. *Geof. Int.,* **40**(3), 181–190.

Jording, A., Ferrari, L., Arzate, J. & Jödicke, H., 2000. Crustal variations and terrane boundaries in southern Mexico as imaged by magnetotelluric transfer functions. *Tectonophysics,* **327**(1–2), 1–13.

Julià, J. & Mejía, J., 2004. Thickness and Vp/Vs ratio variation in the Iberian crust. *Geophys. J. Int.,* **156**(1), 59–72.

Kennett, B.L.N., 1991. IASPEI 1991 Seismological Tables. *Terra Nova,* **3**(2), 1–122.

Kim, Y., Clayton, R.W. & Jackson, J.M., 2010. Geometry and seismic properties of the subducting Cocos plate in central Mexico. *J. geophys. Res.: Solid Earth,* **115**(B6).

Langston, C., 1979. Structure under Mount Rainer, Washington, Inferred by teleseismic body waves. *J. geophys. Res.,* **84,** 4749–4762.

Ligorría, J. & Ammon, C., 1999. Iterative deconvolution and receiver function estimation. *Bull. seism. Soc. Am.,* **89**(5), 1395–1400.

Litak, R.K. & Brown, L.D., 1989. A modern perspective on the Conrad discontinuity. *EOS, Trans. Am. Geophys. Un.,* **70**(29), 713–725.

Marton, G. & Buffler, R.T., 1994. Jurassic reconstruction of the Gulf of Mexico Basin. *Int. Geol. Rev.,* **36**(6), 545–586.

MASE, 2007. Meso America Subduction Experiment. Caltech. Dataset. doi:10.7909/C3RN35SP.

Melgar, D. & Pérez-Campos, X., 2011. Imaging the Moho and subducted oceanic crust at the Isthmus of Tehuantepec, Mexico, from receiver functions. *Pure appl. Geophys.,* **168**(8–9), 1449–1460.

Montealegre-Cázares, C. & Pérez-Campos, X., 2016. Study of the subduction zone in central Mexico by using non-linear and non-stationary analysis (Empirical Mode Decomposition) on receiver functions, *paper presented at the AGU Fall Meeting 2016*, San Francisco, CA, 12–16 December.

Morán-Zenteno, D., Corona-Chavez, P. & Tolson, G., 1996. Uplift and subduction erosion in southwestern Mexico since the Oligocene: pluton geobarometry constraints. *Earth planet. Sci. Lett.,* **141,** 51–65.

Nava, F. *et al.*, 1988. Structure of the Middle America trench in Oaxaca, Mexico. *Tectonophysics,* **154**(3), 241–251.

Ozakin, Y. & Ben-Zion, Y., 2015. Systematic receiver function analysis of the Moho geometry in the Southern California plate-boundary region. *Pure appl. Geophys.,* **172**(5), 1167–1184.

Pérez-Campos, X. *et al.*, 2008. Horizontal subduction and truncation of the Cocos Plate beneath central Mexico. *Geophys. Res. Lett.,* **35**(18), L18303.

Pérez-Campos, X. *et al.*, 2018. The Mexican national seismological service: an overview. *Seismol. Res. Lett.,* **89**(2A), 318–323.

Persaud, P., Pérez-Campos, X. & Clayton, R.W., 2007. Crustal thickness variations in the margins of the Gulf of California from receiver functions. *Geophys. J. Int.,* **170**(2), 687–699.

Saragiotis, C., Hadjileontiadis, L.J., Savvaidis, A.S., Papazachos, C.B. & Panas, S.M., 2000. Automatic S-phase arrival determination of seismic signals using nonlinear filtering and high-order statistics. *Proc. IGARSS,* 1, 292–294.

Saragiotis, C., Hadjileontiadis, L.J. & Panas, S.M., 2002. PAI-S/K: a robust automatic seismic P phase arrival identification scheme. *IEEE Trans. Geosci. Remote Sens.,* **40**(6), 1395–1404.

Sedlock, R.L., Ortega-Gutiérrez, F. & Speed, R.C., 1993. Tectonostratigraphic Terranes and Tectonic Evolution of Mexico, **Vol. 278,** Geological Society of America.

Stern, C.R., 2011. Subduction erosion: rates, mechanisms, and its role in arc magmatism and the evolution of the continental crust and mantle. *Gondwana Res.,* **20,** 284–308.

Sodoudi, F. *et al.*, 2006. Lithospheric structure of the Aegean obtained from P and S receiver functions. *J. geophys. Res.,* **111**(B12307), 1–23.

Spica, Z., Perton, M., Calò, M., Legrand, D., Córdoba-Montiel, F. & Iglesias, A., 2016. 3-D shear wave velocity model of Mexico and South US: bridging seismic networks with ambient noise cross-correlations (C1) and correlation of coda of correlations (C3). *Geophys. J. Int.,* **206**(3), 1795–1813.

SSN, 2018. *Servicio Sismológico Nacional, Instituto de Geofísica,* Universidad Nacional Autónoma de México, México, doi:10.21766/SSNMX/SN/MX.

Stubailo, I., Beghein, C. & Davis, P.M., 2012. Structure and anisotropy of the Mexico subduction zone based on Rayleigh-wave analysis and implications for the geometry of the Trans-Mexican Volcanic Belt. *J. geophys. Res.: Solid Earth,* **117**(B5).

Tian, B.F., Li, J. & Yao, Z.X., 2008. Crustal anisotropy of Taihang Mountain Range using azimuthal variation of receiver functions. *Acta Seismol. Sin.,* **21**(4), 358–369.

Urrutia-Fucugauchi, J. & Flores-Ruiz, J.H., 1996. Bouguer gravity anomalies and regional crustal structure in central Mexico. *Int. Geol. Rev.,* **38**(2), 176–194.

Valdés, C.M. *et al.*, 1986. Crustal structure of Oaxaca, Mexico, from seismic refraction measurements. *Bull. seism. Soc. Am.,* **76**(2), 547–563.

VEOX, 2010. Veracruz-Oaxaca Subduction Experiment. Caltech. Dataset. doi:10.7909/C3MW2F2C.

Vinnik, L., Oreshin, S., Makeyeva, L. & Dündar, S., 2017. Fluid-filled porosity of magmatic underplates from joint inversion of P and S receiver functions. *Geophys. J. Int.,* **209**(2), 961–968.

Wessel, P. & Smith, W.H., 1998. New, improved version of Generic Mapping Tools released. *EOS, Trans. Am. Geophys. Un.,* **79**(47), 579–579.

Wu, Z. & Huang, N.E., 2009. Ensemble empirical mode decomposition: a noise-assisted data analysis method. *Adv. Adapt. Data Anal.,* **1**(01), 1–41.

Yang, T., Grand, S.P., Wilson, D., Guzman-Speziale, M., Gomez-Gonzalez, J.M., Dominguez-Reyes, T. & Ni, J., 2009. Seismic structure beneath the Rivera subduction zone from finite-frequency seismic tomography. *J. geophys. Res.,* **114**(B1), B01302.

Yeck, W.L., Sheehan, A.F. & Schulte-Pelkum, V., 2013. Sequential H-κ stacking to obtain accurate crustal thicknesses beneath sedimentary basins. *Bull. seism. Soc. Am.,* **103**(3), 2142–2150.

Yeh, J.R., Shieh, J.S. & Huang, N.E., 2010. Complementary ensemble empirical mode decomposition: a novel noise enhanced data analysis method. *Adv. Adapt. Data Anal.,* **2**(02), 135–156.

Zhou, L., Chen, W.P. & Ozalaybey, S., 2000. Seismic properties of the central Indian shield. *Bull. seism. Soc. Am.,* **90**(5), 1295–1304.

Zhu, L. & Kanamori, H., 2000. Moho depth variation in southern California from teleseismic receiver functions. *J. geophys. Res.,* **105**(B2), 2969–2980.

SUPPORTING INFORMATION

Supplementary data are available at *GJI* online.

Table S1. List of stations and their corresponding network, location and tectonostratigraphic terrane they belong to. Backazimuthal depth (four subsets of 90°) to three crustal seismic discontinuities: sedimentary layer, Conrad and crustal thickness.

Figure S2-1. Receiver functions for station TUXT ordered by backazimuth. The colour corresponds to their azimuthal group. Enhanced pulses are enclosed with boxes. The area with mixed-pulses is enclosed with an ellipse. (a) Original. (b) Bandpass filter 1.0–5.0 Hz. (c) Bandpass filter 0.1–1.0 Hz. (d) Bandpass filter 0.5–5.0 Hz. (e) IMF-1. (f) IMF-2. (g) IMF-3. (h) IMF-2 + IMF-3.

Figure S2-2. Receiver functions for station PAMA ordered by backazimuth. The colour corresponds to their azimuthal group as in Fig. 1. Enhanced pulses are enclosed with boxes. (a) Original. (b) Bandpass filter 1.0–5.0 Hz. (c) Bandpass filter 0.1–1.0 Hz. (d) Bandpass filter 0.5–5.0 Hz. (e) IMF-1. (f) IMF-2. (g) IMF-3. (h) IMF-2 + IMF-3.

Figure S2-3. Receiver functions for station PAMA ordered by backazimuth. The colour corresponds to their azimuthal group. Enhanced pulses are enclosed with boxes. (a) Original. (b) Bandpass filter 1.0–5.0 Hz. (c) Bandpass filter 0.1–1.0 Hz. (d) Bandpass filter 0.5–5.0 Hz. (e) IMF-1. (f) IMF-2. (g) IMF-3. (h) IMF-2 + IMF-3.

Please note: Oxford University Press is not responsible for the content or functionality of any supporting materials supplied by the authors. Any queries (other than missing material) should be directed to the corresponding author for the paper.